1-1-2018

Epitaxial growth of Ni(OH)2 nanoclusters on MoS2 nanosheets for enhanced alkaline hydrogen evolution reaction

Guoqiang Zhao
University of Wollongong, gz815@uowmail.edu.au

Yue Lin
University of Science and Technology of China

Kun Rui
University of Wollongong, krui@uow.edu.au

Qian Zhou
University of Wollongong, qz704@uowmail.edu.au

Yaping Chen
University of Wollongong, yc463@uowmail.edu.au

See next page for additional authors

Epitaxial growth of Ni(OH)2 nanoclusters on MoS2 nanosheets for enhanced alkaline hydrogen evolution reaction

Abstract

Constructing heterostructures is an effective strategy for designing efficient electrocatalysts. MoS2 is a star catalyst for hydrogen evolution reaction (HER) in acidic media; however, the alkaline HER activity is deficient due to the sluggish water dissociation process. Herein, Ni(OH)2/MoS2 heterostructures with Ni(OH)2 nanoclusters epitaxially decorated on the surface of MoS2 are synthesized towards the alkaline HER. As compared with MoS2, the epitaxial Ni(OH)2/MoS2 heterostructures show significantly enhanced HER activity in 1 M KOH, and the overpotential is decreased by nearly 150 mV to reach a current density of 10 mA cm-2. The substantial increase in turnover frequency (TOF) demonstrates that the intrinsic activity is greatly improved after the incorporation of Ni(OH)2 nanoclusters. The presence of Ni(OH)2 nanoclusters would provide additional water dissociation sites while MoS2 is ready for the adsorption and combination of the generated H*, and this so-called synergistic effect eventually induces significantly enhanced alkaline HER kinetics. Besides, the electron transfer from Ni(OH)2 to MoS2 increases the proton affinity of MoS2. The present results describe an interesting case of an atomic-scale electrochemically inert material promoted HER process, and would open a new avenue into designing efficient hetero-nanostructures towards electrocatalytic applications.

Disciplines

Engineering | Physical Sciences and Mathematics

Publication Details

Zhao, G., Lin, Y., Rui, K., Zhou, Q., Chen, Y., Dou, S. Xue. & Sun, W. (2018). Epitaxial growth of Ni(OH)2 nanoclusters on MoS2 nanosheets for enhanced alkaline hydrogen evolution reaction. Nanoscale, 10 (40), 19074-19081.

Authors

Guoqiang Zhao, Yue Lin, Kun Rui, Qian Zhou, Yaping Chen, Shi Xue Dou, and Wenping Sun

Journal Name

ARTICLE

Epitaxial Growth of $Ni(OH)_2$ Nanoclusters on MoS_2 Nanosheets for Enhanced Alkaline Hydrogen Evolution Reaction†

Received 00th January 20xx,
Accepted 00th January 20xx

DOI: 10.1039/x0xx00000x

www.rsc.org/

Guoqiang Zhao,[a] Yue Lin,*[b] Kun Rui,[a] Qian Zhou,[a] Yaping Chen,[a] Shi Xue Dou,[a] and Wenping Sun*[a]

Constructing heterostructures is an effective strategy for designing efficeint electrocatalysts. MoS_2 is a star catalyst for hydrogen evolution reaction (HER) in acidic media; however, the alkaline HER activity is deficient due to the sluggish water dissociation process. Herein, $Ni(OH)_2/MoS_2$ heterostructures with $Ni(OH)_2$ nanoclusters epitaxially decorated on the surface of MoS_2 are synthesized towards alkaline HER. As compared with MoS_2, the epitaxial $Ni(OH)_2/MoS_2$ heterostructures show significantly enhanced HER activity in 1M KOH, and the overpotential is decreased by nearly 150 mV to reach a current density of 10 mA cm^{-2}. The substantial increase in turnover frequency (TOF) demonstrates that the intrinsic activity is greatly improved after the incorporation of Ni(OH)2 nanoclusters. The presence of $Ni(OH)_2$ nanoclusters would provide additional water dissociation sites while MoS_2 is ready for the adsorption and combination of the generated H^*, and this so-called synergistic effect eventually induces significantly enhanced alkaline HER kinetics. Besides, the electron transfer from $Ni(OH)_2$ to MoS_2 increases the proton affinity of MoS_2. The present results describe an interesting case of atomic-scale electrochemically inert material promoted HER process, and would open a new avenue into designing efficient hetero-nanostructures towards electrocatalysis applications.

Introduction

Heterostructures have received extensive attention in recent years due to their potential applications in a variety of research fields, such as semiconductors, sensors, photoelectric devices, and electrochemical catalysts.[1-3] The abundant interfaces in heterostructures usually possess unique physicochemical properties as compared with their single-component counterparts.[4, 5] To date, heterostructures based on transition metal dichalcogenides (TMDs) are being developed rapidly toward electrochemical water splitting, especially for hydrogen evolution reaction (HER) in acidic media.[3, 6] On the one hand, 2D TMDs usually possess high intrinsic activities owing to the moderate binding energy to hydrogen or partially-filled E_g band.[7, 8] On the other hand, constructing heterostructures is helpful for exposing more active sites,[9-12] modulating the electronic structures at the interfaces,[13] and inducing synergistic effects between different components.[3, 13-15] Therefore, TMD-based heterostructures usually exhibit greatly enhanced HER catalytic activity over the bare TMDs catalysts.

Compared with the HER in acid media where protons directly come from the solution, the alkaline HER is more complicated since protons are provided by splitting water molecules. Consequently, the reaction kinetics of alkaline HER is severely impeded by the initial water dissociation step, and the overall reaction kinetics is generally two to three orders of magnitude lower than that in acidic media.[16] Although TMD-based heterostructures have been successfully demonstrated in acid media, developing advanced TMD-based heterostructured catalysts toward alkaline HER is still in its infancy. Despite the moderate hydrogen binding energies that they may possess, most TMDs are usually not favorable for the water adsorption/dissociation process.[17, 18] Thus, decorating TMDs with a second phase with an appropriate water binding energy is an efficient strategy to boost alkaline HER activity.

Recently, it was reported that $Ni(OH)_2$ can promote the alkaline HER activity of various metal electrodes. The promotion is ascribed to the synergistic effect between $Ni(OH)_2$ and metal catalysts, where $Ni(OH)_2$ breaks water molecules and the generated hydrogen subsequently adsorbs on metal surfaces.[19-22] Similar activity improvement induced by $Ni(OH)_2$ was also demonstrated in other types of materials.[23-25] However, it is worth noting that $Ni(OH)_2$ is catalytically inert for HER and it only works for dissociating water molecules. Thus, the ideal situation is to minimize the content of $Ni(OH)_2$ in order to achieve the optimal mass-based activity. In this work, we synthesized $Ni(OH)_2/MoS_2$ heterostructures with atomic-scale $Ni(OH)_2$ clusters epitaxially deposited on the surface of MoS_2. Although the content of $Ni(OH)_2$ is low, the

[a] Institute for Superconducting and Electronic Materials, Australian Institute for Innovative Materials, University of Wollongong, Wollongong, NSW 2522, Australia. Email: wenping@uow.edu.au
[b] Hefei National Laboratory for Physical Sciences at the Microscale Institution, University of Science and Technology of China, Hefei, Anhui 230026, P. R. China. Email: linyue@ustc.edu.cn

† Electronic Supplementary Information (ESI) available: [The synthetic process illustration, SEM image of pure MoS_2, additional HAADF-STEM image of 0.2NM, XRD patterns, the fitted Ni 2p XPS plot, LSV curves of pure MoS_2, TEM image of 0.2NM after stability test, CV curves for evaluating C_{dl}, fitted equivalent elements for EIS, HER activities of reported electrocatalysts in alkaline media]. See

$Ni(OH)_2/MoS_2$ heterostructures still showed significantly enhanced alkaline HER activity as compared with bare MoS_2. The present results provide new insights into understanding the alkaline HER mechanism of TMD-based heterostructures and shed light on designing efficient hetero-nanostructures towards electrocatalysis applications.

Experimental section

Synthetic procedures

All chemicals were purchased from Sigma-Aldrich (A.R) and were used as received without further purification. Ultrapure deionized water (18 MΩ cm^{-1}) was used in all experiments.

Preparation of MoS_2: MoS_2 was prepared through a hydrothermal method. In a typical synthetic procedure, 1.235 g (1 mmol) $(NH_4)_6Mo_7O_{24}{\cdot}4H_2O$ and 1.065 g (14 mmol) CH_4N_2S were dissolved in 35mL deionized water (DI-water) under continuous stirring. The obtained solution was transferred to a stainless-steel autoclave with a 50 mL Teflon liner, and the autoclave was sealed and maintained at 180 °C for 30 h in an oven. After cooling to room temperature, the precipitates were washed with ethanol (EtOH) and de-ionized water (DI-water) several times and collected by centrifugation. The obtained powders were dried at 60 °C in vacuum overnight to get the MoS_2 nanosheets.

Preparation of $Ni(OH)_2/MoS_2$ heterostructures and bare $Ni(OH)_2$: Typically, 45 mg MoS_2 powders were dispersed in 15 mL EtOH and treated with ultrasonication for 3 h. Stoichiometric amounts of $NiCl_2$ and CH_4N_2O were dissolved into the suspension together with 5 mL DI-water and 20 mL ethylene glycol (EG), and then the suspensions were transferred to a three-neck flask. The flask was then heated on a stirring heater at 96 °C for 2 h under reflux condition and cooled to room temperature naturally. The precipitates were washed with EtOH and DI-water several times and collected by centrifugation. After drying at 60 °C in vacuum overnight, the final products were obtained.

The bare $Ni(OH)_2$ was prepared via the same processes as preparing $Ni(OH)_2/MoS_2$ heterostructures except that no MoS_2 nanosheets were added.

Materials Characterization

The X-ray diffraction (XRD) patterns were recorded using a GBC enhanced mini-materials analyzer X-Ray diffractometer with a $Cu_{K\alpha}$ radiation (λ=1.541 Å, 25 mA, 40 kV, 2 °min^{-1} from 10 ° to 70 °). The materials surface chemical state was detected by X-ray photoelectron spectroscopy (XPS, Phoibos 100 Analyser, SPECS, Germany, $Al_{K\alpha}$ X-rays). Raman spectra were performed using a Raman JY HR800 Spectrometer with a 632.8nm He-Ne gas laser with spectral resolution down to 0.35 cm^{-1}. The samples morphologies were characterized by a JEOL JSM-7500FA field-emission scanning electron microscope (FESEM) at an accelerating voltage of 5 kV. High angle annular dark field scanning transmission electron microscopy (HAADF-STEM) images were acquired on a probe-corrected JEOL ARM200F TEM operated at 80 kV equipped with a thermal field emission gun and an ultrahigh resolution pole-piece. Energy disperse X-ray mappings (EDS) were acquired on FEI Talos F200X equipped with four symmetrical EDS signal detectors, operated at 200 kV.

Electrochemical tests

Electrochemical tests were conducted with a rotating disc electrode (RDE) systems in 1 M KOH aqueous solution using a standard three-electrode electrochemical cell. A Pt mesh and a Hg/HgO electrode were employed as the counter and reference electrode, respectively. For preparing working electrodes, 4 mg catalysts were dispersed in 1 mL testing solution containing 32 μL Nafion solution (5 wt%), 768 uL DI-water, and 200 uL isopropanol by 3 h ultrasonication to form a homogeneous ink. Then 10 μL catalyst ink (containing 40 μg of catalyst) was loaded onto a GC electrode (mass loading ~ 0.204 mg cm^{-2}) and dried naturally in the ambient air. Electrochemical experiments were controlled by a WaveDriver 20 potentiostat (Pine Research Instruments, US). Prior to HER tests, the KOH solution was bubbled with high-purity nitrogen for at least 30 min to remove dissolved oxygen. During the measurements, the working electrode was constantly rotating at 1600 rpm to alleviate diffusion. All potentials reported are referenced to the reversible hydrogen electrode (RHE), and the ohmic potential drop caused by the solution resistance has been compensated with 95% iR-correction.

Linear sweep voltammetry (LSV) was performed at 5 mV s^{-1} from 0 to -0.5 V vs. RHE. The stability of the catalysts was evaluated by cyclic voltammetry (CV) carried out at a scan rate of 100 mV s^{-1} for 1000 cycles. Electrochemical impedance spectra (EIS) was measured at various potentials in the frequency range of 100 kHz~10 mHz at the amplitude voltage of 10 mV.

Calculation of the double-layer capacitance

The materials electrochemically active surface area (ECSA) is evaluated by calculating the double-layer capacitance (C_{dl}) of the electrodes. Cyclic voltammetry (CV) was performed in a potential range from -50 ~ 50 mV vs. RHE at 40, 80, 120, 160 and 200 mV s^{-1} to evaluate the capacitive behavior of the electrodes, then C_{dl} was calculated according to Eq. 1.

$$C_{dl} = \frac{|j_a| + |j_c|}{2\nu} \quad (1)$$

j_a—anodic current density, mA cm^{-2}

j_c—cathodic current density, mA cm^{-2}

ν—scan rate, mV s^{-1}

Calculation of the turnover frequency (TOF)

According to the definition, the number of H_2 molecules generated per second and the number of active sites should be determined to calculate TOF (Eq. 2). The total number of H_2 molecules generated per second can be obtained from Faraday's law of electrolysis (Eq. 3) assuming 100% Faradic efficiency. The surface Mo atom is introduced to evaluate the number of active sites, which is estimated to be $1.46{\times}10^{15}$ cm^{-2}

for MoS_2 based on its lattice constants. For the $Ni(OH)_2/MoS_2$ heterostructures, the surface Mo atom numbers are estimated based on the real Mo atom density in the heterostructures deduced from XPS results.

$$TOF=\frac{\text{Generated } H_2 \text{ molecule number per second}}{\text{Number of active sites}} \quad (2)$$

$$N_{H_2}=\frac{Q}{2F}\times N_A=\frac{j\times t}{1000}\times\frac{1}{2F}\times N_A \quad (3)$$

N_{H_2} —molecule number of H_2
Q—quantity of electric charge, C
F—Faraday's constant, 96485 C/mol
N_A—Avogadro constant, 6.02×10^{23}
j—HER current density, mA cm^{-2}
t—unit time, 1 s

Results and discussion

The $Ni(OH)_2/MoS_2$ heterostructures were prepared via a two-step solution-phase method, as illustrated in Fig. S1†. The obtained samples were noted as 0.05NM, 0.2NM, and 0.5NM based on the theoretical Ni/Mo molar ratio. Taking 0.2NM as an example, the molar ratio of $NiCl_2$ to MoS_2 is 0.2:1 during the reflux process. As shown in Fig. 1a, the 0.2NM heterostructure inherits the typically curved nanosheet morphology of MoS_2 (Fig. S2†), which is further revealed by the low-magnification HAADF-STEM image as shown in Fig. 1b. The EDS mapping images illustrate a uniform distribution of Mo, S, Ni and O (Fig.

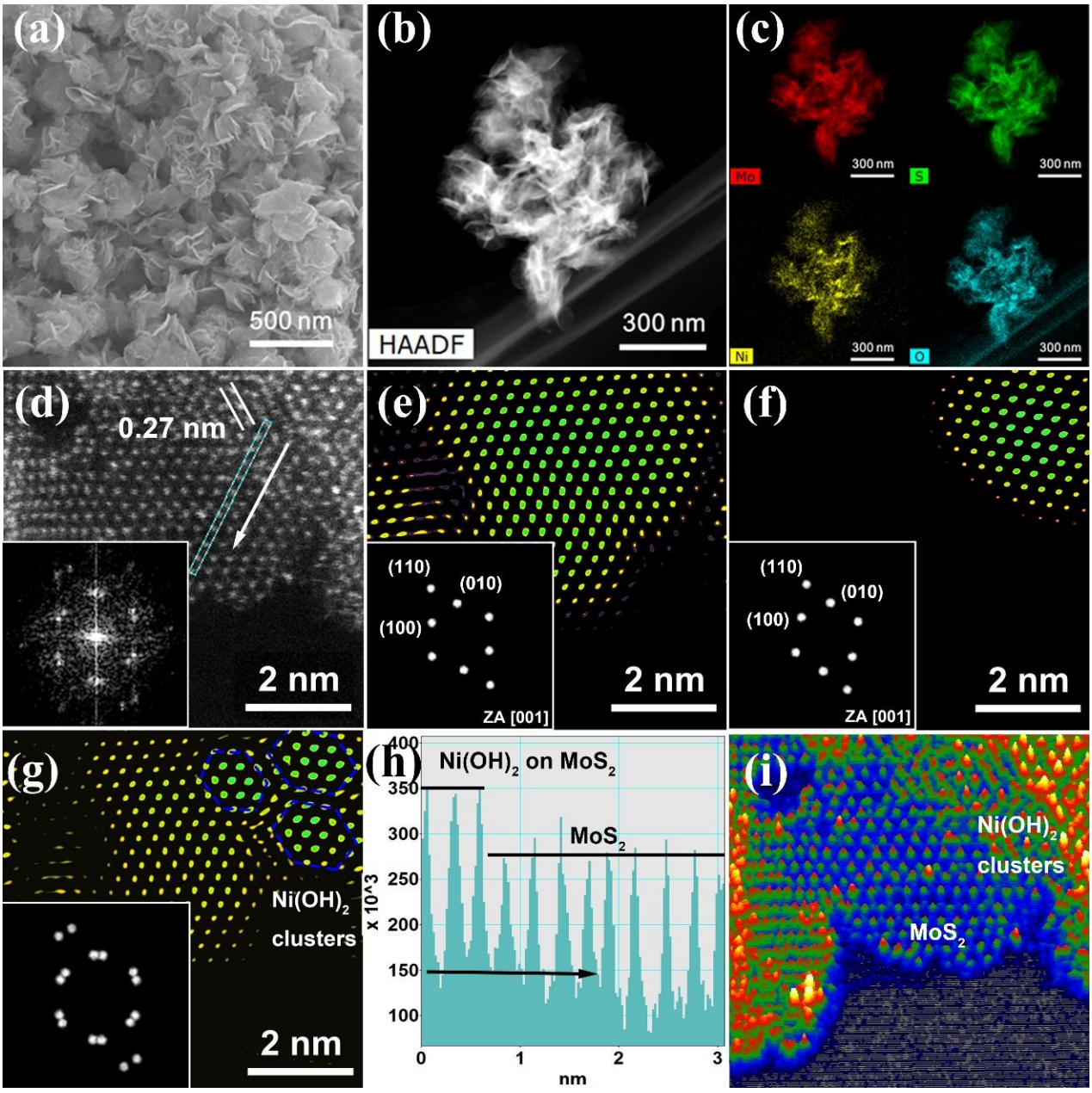

Fig. 1 (a) SEM image of 0.2NM. (b) HAADF-STEM image of 0.2NM. (c) EDS mapping images of 0.2NM. (d) HAADF-STEM image of 0.2NM, the arrow indicates the direction of the intensity profile, and the inset is the corresponding FFT patterns. IFFT image of (e) MoS_2 matrix, (f) $Ni(OH)_2$ cluster, and (g) 0.2NM generated by the selected masked FFT spots. Insets: the selected FFT spots. (h) Intensity profiles correspond to (d). (i) The surface plot image of (d).

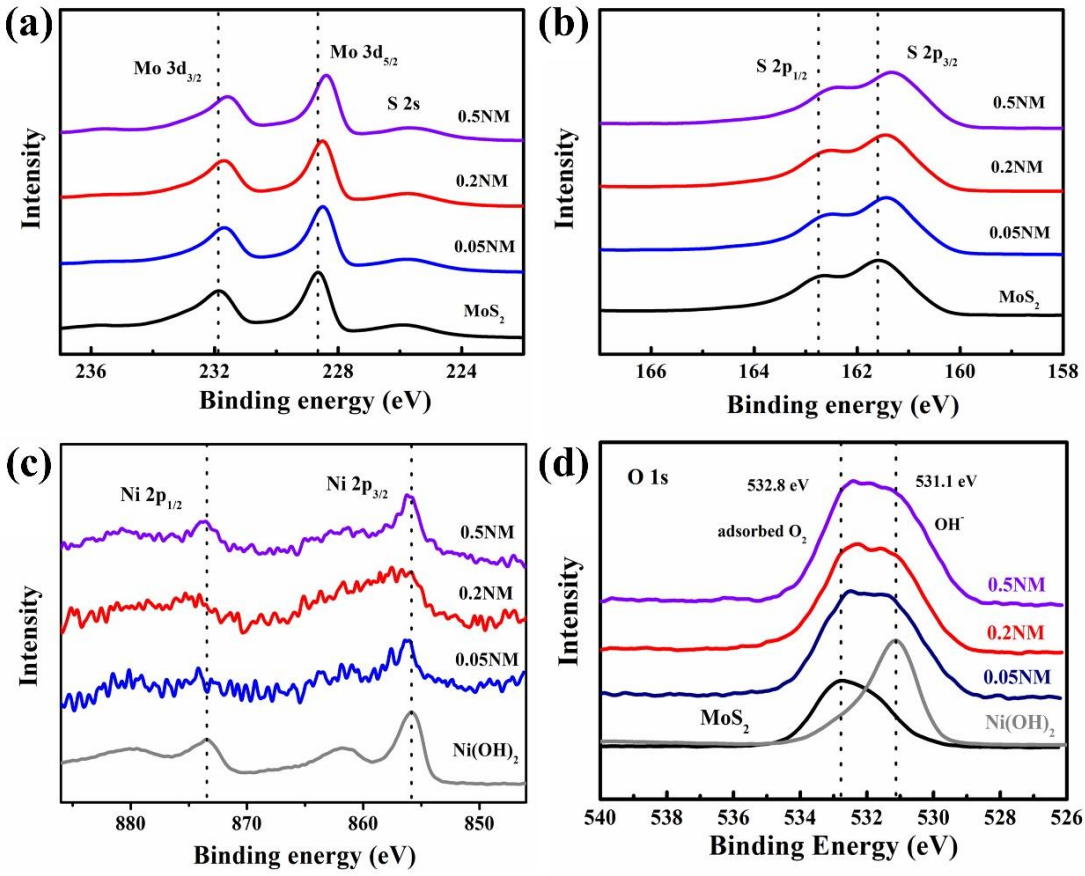

Fig. 2 High-resolution XPS spectra of (a) Mo 3d, (b) S 2p, (c) Ni 2p, and (d) O 1s.

1c), demonstrating the homogeneous dispersion of $Ni(OH)_2$ species over MoS_2 surface. Also, the Ni/Mo atomic ratio for 0.2NM is calculated to be 8% based on the quantitative EDS analysis. In Fig. 1d, the high-magnification HAADF-STEM image of 0.2NM shows a typical lattice fringe with a spacing of 0.27 nm, which could be ascribed to either MoS_2 or $Ni(OH)_2$ since their cell parameters are too close to be distinguished. However, two sets of FFT spots are shown in the corresponding fast Fourier Transformation (FFT) pattern in the inset in Fig. 1d. Both sets of FFT spots can be indexed to typical hexagonal structures along [001] zone axis with slight lattice mismatch (2%) and angular misorientation (9 °). By applying inversed FFT (IFFT) on the selected FFT spots, two patterns are regenerated and displayed in Fig. 1e and f. Specifically, the lattice fringes of {100} planes in Fig. 1e and f are calculated to be 0.272 and 0.267 nm, which can be assigned to the MoS_2 substrate and $Ni(OH)_2$ species, respectively. The reassembled FFT patterns and the corresponding IFFT image are displayed in Fig. 1g, which resembles Fig. 1d. The small lattice mismatch and angular misorientation between $Ni(OH)_2$ and MoS_2 demonstrate the epitaxial relationship between $Ni(OH)_2$ nanoclusters and MoS_2, where $[100]_{Ni(OH)2} \| [100]_{MoS2}$ and $(100)_{Ni(OH)2} \| (100)_{MoS2}$. It is also worth noting that such tiny lattice difference between $Ni(OH)_2$ and MoS_2 is actually beyond the resolution of the TEM, and additional evidence has to be employed to locate $Ni(OH)_2$ clusters. To address this issue, we analyze the intensity of the heterostructure based on the z-contrast of the HAADF-STEM image,[26, 27] where the intensity in the image is proportional to the square of atomic numbers.[28] Fig. 1h is the intensity profile of the path labelled in Fig. 1d, and the arrows indicate the direction of the path. Calculations demonstrate that the intensity ratio of the proposed $Ni(OH)_2/MoS_2$ heterostructure is in good accordance with the theoretical values. Similar results can also be found in Fig. S3†, and the detailed calculation process can be found in Note S1†. The surface plot of the heterostructure is shown in Fig. 1i, further illustrating the $Ni(OH)_2/MoS_2$ heterostructure. Based on these analysis, the $Ni(OH)_2$ species possess an atomic-scale cluster morphology with an average size of 2~5 nm.

XRD patterns are shown in Fig. S4†. For MoS_2, the broad peaks at 22.7 ° and 58.3 ° can be indexed to the (100) and (110) planes of hexagonal MoS_2 (JCPDS # 37-1492). The diffraction peaks at 11.4 °, 33.9 °, and 60.2 ° in $Ni(OH)_2$ spectra can be attributed to the (003), (101), and (110) planes of α-phase $Ni(OH)_2$ (JCPDS # 89-7111). However, the low loading content, poor crystallinity, and the ultra-small size of the $Ni(OH)_2$ nanoclusters result in low XRD intensity; therefore, the XRD patterns of $Ni(OH)_2/MoS_2$ heterostructures are dominated by MoS_2 substrates, and no characteristic diffraction peaks of $Ni(OH)_2$ is observed. The chemical compositions of the samples were characterized by XPS. For bare MoS_2, the two peaks with binding energies of 228.7 and 231.9 eV in Fig. 2a correspond to Mo $3d_{5/2}$ and Mo $3d_{3/2}$, respectively; and the two peaks

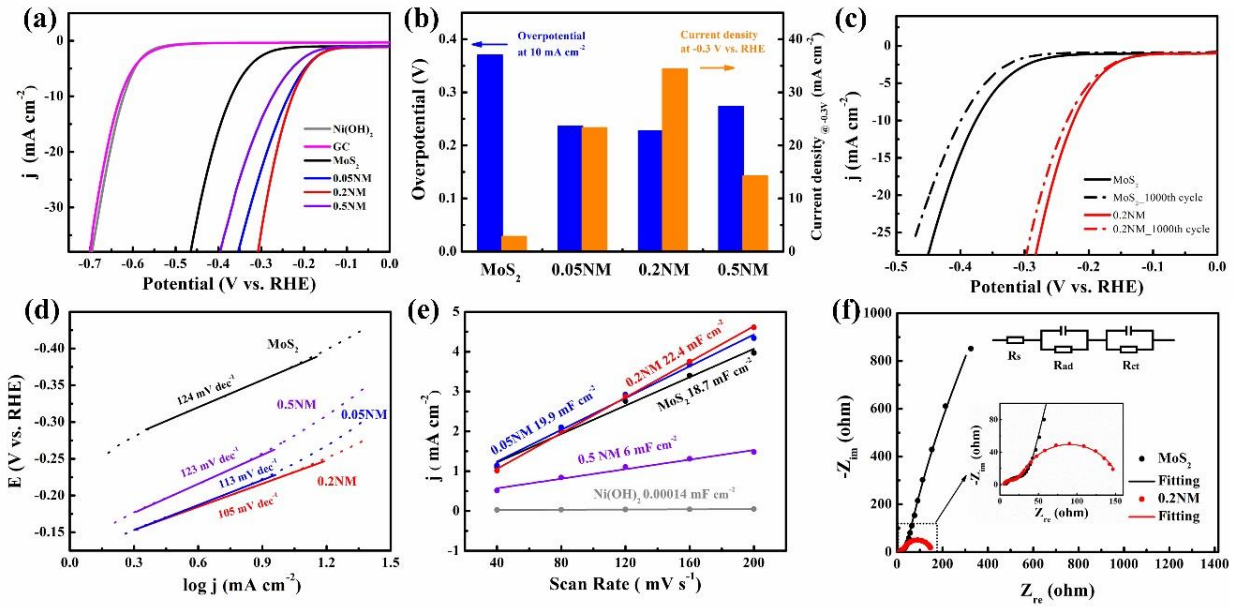

Fig. 3. (a) LSV curves of the samples as indicated. (b) The overpotential at the current density of 10 mA cm^{-2} and the current densities at the overpotential of 300 mV of the sampels. (c) LSV curves of MoS_2 and 0.2NM measured before and after 1000 CV cycles. (d) Tafel plots of the samples as indicated. (e) Calculated C_{dl} for the samples. (f) Nyquist plots of MoS_2 and 0.2NM, and the equivalent circuit used for fitting

located at 161.6 and 162.7 eV in Fig. 2b can be assigned to S $2p_{3/2}$ and S $2p_{1/2}$, respectively.[29] In Fig. 2c, two major peaks corresponding to Ni $2p_{3/2}$ and Ni $2p_{1/2}$ are observed at 855.8 and 873.5 eV, and two satellite peaks at 861.8 and 879.7 eV are found in the spectra of bare $Ni(OH)_2$.[30] In Fig. 2d, the characteristic O 1s peak of $Ni(OH)_2$ is found at 531.1 eV,[31] while the peak at 532.8 eV in the spectra of MoS_2 is originated from the adsorbed O_2 on MoS_2 surface.[32] For the $Ni(OH)_2/MoS_2$ heterostructures, O 1s peaks derived from both the adsorbed O_2 and the $Ni(OH)_2$ species could be clearly observed and fitted (Fig. S5†), which also confirms the existence of $Ni(OH)_2$ species. Moreover, the binding energies of both Mo and S shift negatively in the $Ni(OH)_2/MoS_2$ heterostructures, while the binding energies of Ni move positively compared with bare $Ni(OH)_2$. Particularly, for 0.2NM, the binding energies of Mo and S decrease about 0.3 eV compared with bare MoS_2, while the binding energy of Ni increases 1.8 eV compared with bare $Ni(OH)_2$. In general, this variation in binding energies demonstrates a strong electronic interaction between the components. In this case, electron transfer from $Ni(OH)_2$ to MoS_2 is suggested,[10, 33] which will increase the electron density and enhance the proton affinity of MoS_2, resulting in higher HER activity.[34] On the other hand, such electron transfer will lower the energy gap between the highest occupied molecular orbital (HOMO) of MoS_2 and the lowest unoccupied molecular orbital (LUMO) of the absorbed hydrogen and hence accelerate the charge transfer process.[35, 36] In addition, XPS results also indicate a Ni/Mo molar ratio of 8% for 0.2NM, which is in perfect consistency with the quantitative EDS analysis.

The HER performance was evaluated in N_2-saturated 1M KOH solution using a standard three-electrode electrochemical cell. All the presented LSV data were obtained at a scan rate of 5 mV s^{-1} and were corrected with 95% iR compensation. Fig. 3a shows LSV curves of $Ni(OH)_2/MoS_2$ heterostructures, MoS_2, $Ni(OH)_2$, and bare GC. Specifically, the LSV curve of $Ni(OH)_2$ is almost identical to bare GC, and the required overpotential to reach a current density of 10 mA cm^{-2} is higher than 600 mV, indicating that $Ni(OH)_2$ is electrochemically inert for alkaline HER. For MoS_2, the overpotential at 10 mA cm^{-2} is 370 mV in 1M KOH, which is much higher than that in acidic media (Fig. S6†) due to the sluggish reaction kinetics of water dissociation.[19] After decorating with $Ni(OH)_2$ nanoclusters, the catalytic activity of MoS_2 is substantially improved. As shown in Fig. 3b, to reach a current density of 10 mA cm^{-2}, the overpotential is decreased to only 236, 227 and 273 mV for 0.05NM, 0.2NM, and 0.5NM, respectively. At an overpotential of 300 mV, the current density is only 2.8 mA cm^{-2} for MoS_2, whereas the value reaches 34.4 mA cm^{-2} for 0.2NM, which is more than 10 times that of MoS_2. It is interesting that the catalytically inert $Ni(OH)_2$ with such a low content can induce such significant enhancement in alkaline HER activity, which can be partly ascribed to the atomic-scale $Ni(OH)_2$ cluster that helps to achieve a uniform dispersion. The 0.2NM heterostructure also shows better stability than MoS_2 in 1 M KOH as demonstrated in Fig. 3c. The LSV curve of 0.2NM obtained after 1000 CV cycles shows a tiny shift compared with the initial one. The heterostructure also reserve similar nanosheets morphology after the stability test (Fig. S7†). However, for MoS_2, the overpotential at 10 mA cm^{-2} increases by 20 mV after 1000 CV cycles, which could be caused by the deactivation effect of OH^-.[37]

Tafel slopes are obtained by fitting the Tafel plots in Fig. 3d to get a deeper insight into the catalytic mechanism. A large Tafel slope of 124 mV dec^{-1} is obtained for MoS_2, indicating that the rate determining step (RDS) is the Volmer step in which water molecules break into protons and hydroxyls (OH^-). However, neither the edges nor basal planes of MoS_2 are favored for the

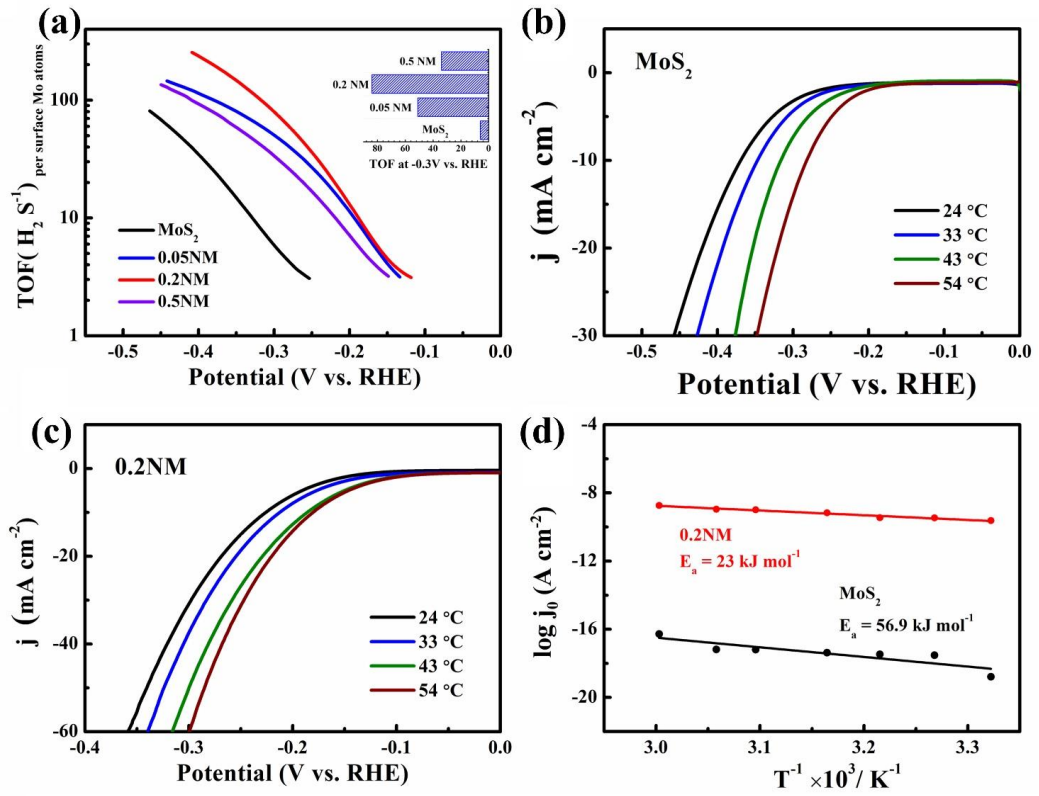

Fig. 4. (a) TOF vs. potential plots for the samples. LSV curves of (b) MoS_2 and (c) 0.2NM at different temperatures. (d) The Arrhenius-type semi-logarithmic plot of current density on inverse temperature.

water adsorption/dissociation.[18] As a result, the sluggish water dissociation process significantly hindered the alkaline HER activity of MoS_2. Compared with MoS_2, the Tafel slope of 0.2NM decreased to 105 mV dec^{-1}, indicating an accelerated water dissociation process. Moreover, the HER inertness of $Ni(OH)_2$ is probably due to the lack of adsorption sites for hydrogen. Fig. 3e shows the double-layer capacitance (C_{dl}) of catalysts deduced form CV curves at various sweep rates (Fig. S8†), which is commonly used as a descriptor for the ECSA. The extremely small C_{dl} (1.44×10^{-4} mF cm^{-2}) of $Ni(OH)_2$ indicates a negligible hydrogen adsorption capability, whereas the large C_{dl} (18.7 mF cm^{-2}) of MoS_2 demonstrates its superior capability for hydrogen adsorption. Both 0.05NM and 0.2NM exhibit similar ECSA to MoS_2, but the ECSA decreases significantly for 0.5NM due to excessive coverage of catalytically inert $Ni(OH)_2$. Notably, 0.5NM delivers better HER performance than MoS_2 despite the lower ECSA, suggesting that the catalytic activity is synergistically determined by the active sites for water adsorption/dissociation and hydrogen adsorption. EIS were measured to further explore the different electrochemical behavior induced by inert $Ni(OH)_2$. Fig. 3f shows the Nyquist plots of 0.2NM and MoS_2 at -200 mV vs. RHE. Both spectra consist of a semicircle at high frequency which represents the hydrogen adsorption behavior and a semicircle at low frequency that is associated with the charge transfer process.[38] The spectra are fitted with an equivalent circuit shown in Fig. 3f, and the fitted results are listed in Table S1†. Compared with MoS_2, 0.2NM exhibits a primarily decreased charge transfer resistance (R_{ct}), demonstrating an accelerated faster charge transfer process after the incorporation of $Ni(OH)_2$.

The TOF was calculated to investigate the intrinsic activity of the catalysts. The number of surface Mo atoms was employed as the number of active sites.[39] The TOF versus overpotential plots are obtained by reforming LSV curves, as shown in Fig. 4a. Compared with MoS_2, the 0.2NM heterostructure shows much higher TOF values and the required overpotential to reach the same TOF decreased nearly 150 mV. At an overpotential of 300 mV, the TOF of MoS_2 is only 6 s^{-1}, whereas the TOF of 0.2 NM increases to 84 s^{-1}, more than 10 times

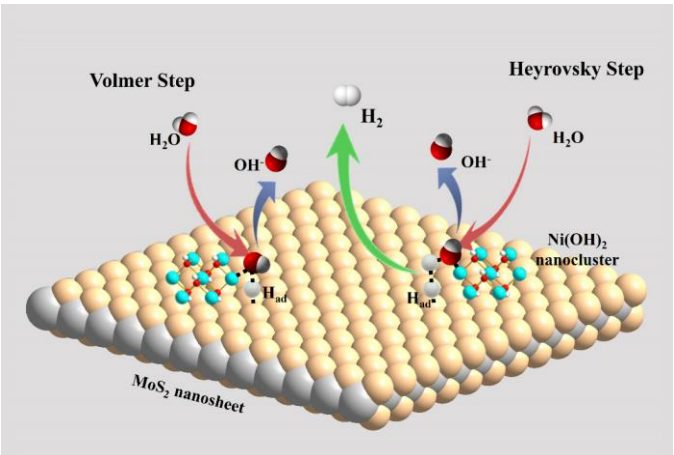

Fig. 5. Illustration of the HER mechanism on $Ni(OH)_2/MoS_2$ surface in alkaline media, showing the synergistic effect between $Ni(OH)_2$ and MoS_2.

higher than that of MoS_2. The large TOF values demonstrate high intrinsic activity of $Ni(OH)_2/MoS_2$ heterostructures, which is comparable to the most advanced noble-metal-free catalysts in alkaline media as listed in Table S2†. It should be mentioned that the catalysts grown on macroscopic substrates (e.g. nickel foam, carbon cloth, etc.) generally exhibit much higher activity than the catalysts deposited on GC electrode, and the most important reason is perhaps the much higher catalyst mass loading rather than intrinsic activity.[3]

To obtain deeper insights into the enhanced intrinsic activity, LSV curves were obtained at a temperature range from 298 K to 330 K as shown in Fig. 4b and c. Both the bare MoS_2 and 0.2NM show enhanced catalytic activity at higher temperatures. The exchange current densities of the HER were calculated based on the corresponding Tafel slopes, and the obtained exchange current densities are plotted in a semi-logarithmic coordinate with the reciprocal of temperature as shown in Fig. 4d. Based on the Arrhenius law, the apparent activation energy is calculated to be 56.9 kJ mol^{-1} (0.59 eV) for MoS_2, which is close to those previously reported results.[40, 41] For 0.2NM heterostructure, the apparent activation energy decreases to 23 kJ mol^{-1} (0.24 eV). Clearly, a decreased apparent activation energy means a low energy barrier and hence an easier reaction process. The overall reaction process can be illustrated in Fig. 5. Due to the presence of the $Ni(OH)_2$ nanoclusters, the water dissociation process is substantially promoted, and the generated hydrogen can subsequently adsorb on the exposed MoS_2 surface; meanwhile, the $Ni(OH)_2$ nanoclusters also accelerate the Heyrovsky step of the HER, in which process the generated hydrogen atom combined with an adsorbed hydrogen atom to form a hydrogen molecule. This synergistic effect between $Ni(OH)_2$ and MoS_2 endows the enhanced HER performance of the $Ni(OH)_2/MoS_2$ heterostructures in alkaline media.

Conclusions

In summary, we synthesized $Ni(OH)_2/MoS_2$ heterostructures with $Ni(OH)_2$ nanoclusters epitaxially grown on the surface of MoS_2 towards enhanced alkaline HER. Detailed analyses reveal the epitaxial relationship between $Ni(OH)_2$ nanoclusters and MoS_2, where $[100]_{Ni(OH)2} \| [100]_{MoS2}$ and $(100)_{Ni(OH)2} \| (100)_{MoS2}$. Although $Ni(OH)_2$ is electrochemically inert for HER, the alkaline HER activity of MoS_2 is substantially promoted by a low content of $Ni(OH)_2$. As compared with MoS_2, the required overpotential to reach a current density of 10 mA cm^{-2} is decreased by nearly 150 mV for the optimized heterostructure, and the TOF at an overpotential of 300 mV is increased by more than 10 times. The incorporation of $Ni(OH)_2$ nanoclusters can not only promote the water adsorption/dissociation process but also modulate the electronic structure of MoS_2, and eventually the synergistic effect between MoS_2 and $Ni(OH)_2$ induces substantially enhanced alkaline HER kinetics. The results represent an effective strategy for preparing heterostructures with atomic-scale second phases and would open a new avenue into designing efficient hetero-nanostructures towards energy applications.

Conflicts of interest

There are no conflicts to declare.

Acknowledgements

This work was financially supported by the Australian Research Council (ARC) DECRA Grant (DE160100596), AIIM FOR GOLD Grant (2017, 2018). Y. Lin thanks supports from the Young Scientists Fund of the National Natural Science Foundation of China (11404314), and Anhui Provincial Natural Science Foundation (1708085MA06). The authors also acknowledge use of facilities within the UOW Electron Microscopy Centre.

Notes and references

1. Q. H. Wang, K. Kalantar-Zadeh, A. Kis, J. N. Coleman and M. S. Strano, *Nat. Nanotechnol.*, 2012, **7**, 699-712.
2. D. Jariwala, T. J. Marks and M. C. Hersam, *Nat. Mater.*, 2017, **16**, 170-181.
3. G. Zhao, K. Rui, S. X. Dou and W. Sun, *Adv. Funct. Mater.*, 2018, DOI: doi:10.1002/adfm.201803291, 1803291.
4. Y. Pan, Y. Chen, Y. Lin, P. Cui, K. Sun, Y. Liu and C. Liu, *J. Mater. Chem. A*, 2016, **4**, 14675-14686.
5. Y. Lin, Y. Pan, J. Zhang, Y. Chen, K. Sun, Y. Liu and C. Liu, *Electrochim. Acta*, 2016, **222**, 246-256.
6. Y. Zhang, Q. Zhou, J. Zhu, Q. Yan, S. X. Dou and W. Sun, *Adv. Funct. Mater.*, 2017, **27**, 1702317.
7. A. Ruban, B. Hammer, P. Stoltze, H. L. Skriver and J. K. Nørskov, *J. Mol. Catal. A: Chem.*, 1997, **115**, 421-429.
8. F. Wang, T. A. Shifa, X. Zhan, Y. Huang, K. Liu, Z. Cheng, C. Jiang and J. He, *Nanoscale*, 2015, **7**, 19764-19788.
9. Y. Chen, Q. Zhou, G. Zhao, Z. Yu, X. Wang, S. X. Dou and W. Sun, *Adv. Funct. Mater.*, 2018, **28**, 1705583.
10. Z. Xing, X. Yang, A. M. Asiri and X. Sun, *ACS Appl Mater Interfaces*, 2016, **8**, 14521-14526.

11. Y. Lin, Y. Pan and J. Zhang, *Electrochim. Acta*, 2017, **232**, 561-569.
12. Y. Pan, Y. Liu, Y. Lin and C. Liu, *ACS Appl. Mater. Interfaces*, 2016, **8**, 13890-13901.
13. M. Wu, Y. Huang, X. Cheng, X. Geng, Q. Tang, Y. You, Y. Yu, R. Zhou and J. Xu, *Adv. Mater. Interfaces*, 2017, **4**, 1700948.
14. J. Li, J. Kang, Q. Cai, W. Hong, C. Jian, W. Liu and K. Banerjee, *Adv. Mater. Interfaces*, 2017, **4**, 1700303.
15. Y. Pan, Y. Lin, Y. Liu and C. Liu, *Catal. Sci. Technol.*, 2016, **6**, 1611-1615.
16. J. Staszak-Jirkovský, C. D. Malliakas, P. P. Lopes, N. Danilovic, S. S. Kota, K.-C. Chang, B. Genorio, D. Strmcnik, V. R. Stamenkovic and M. G. Kanatzidis, *Nat. Mater.*, 2016, **15**, 197.
17. J. Zhang, T. Wang, P. Liu, S. Liu, R. Dong, X. Zhuang, M. Chen and X. Feng, *Energy Environ. Sci.*, 2016, **9**, 2789-2793.
18. K. K. Ghuman, S. Yadav and C. V. Singh, *J. Phys. Chem. C*, 2015, **119**, 6518-6529.
19. N. Danilovic, R. Subbaraman, D. Strmcnik, K. C. Chang, A. Paulikas, V. Stamenkovic and N. M. Markovic, *Angew. Chem.*, 2012, **124**, 12663-12666.
20. S. Anantharaj, K. Karthick, M. Venkatesh, T. V. S. V. Simha, A. S. Salunke, L. Ma, H. Liang and S. Kundu, *Nano Energy*, 2017, **39**, 30-43.
21. R. Subbaraman, D. Tripkovic, K. C. Chang, D. Strmcnik, A. P. Paulikas, P. Hirunsit, M. Chan, J. Greeley, V. Stamenkovic and N. M. Markovic, *Nat Mater*, 2012, **11**, 550-557.
22. M. Chhetri, S. Sultan and C. Rao, *Proceedings of the National Academy of Sciences*, 2017, **114**, 8986-8990.
23. B. Zhang, J. Liu, J. Wang, Y. Ruan, X. Ji, K. Xu, C. Chen, H. Wan, L. Miao and J. Jiang, *Nano Energy*, 2017, **37**, 74-80.
24. X. Zhang and Y. Liang, *Adv. Sci.*, 2018, **5**, 1700644.
25. L. Xie, X. Ren, Q. Liu, G. Cui, R. Ge, A. M. Asiri, X. Sun, Q. Zhang and L. Chen, *J. Mater. Chem. A*, 2018, **6**, 1967-1970.
26. J. M. LeBeau, S. D. Findlay, L. J. Allen and S. Stemmer, *Phys. Rev. Lett.*, 2008, **100**, 206101.
27. Z. Wang, Z. Li, S. Park, A. Abdela, D. Tang and R. Palmer, *Physical Review B*, 2011, **84**, 073408.
28. L. Brown, York, United Kingdom, 2014.
29. N. McIntyre, P. Spevack, G. Beamson and D. Briggs, *Surf. Sci.*, 1990, **237**, L390-L397.
30. K. Lian, D. Kirk and S. Thorpe, *J. Electrochem. Soc.*, 1995, **142**, 3704-3712.
31. A. Venezia, R. Bertoncello and G. Deganello, *Surf. Interface Anal.*, 1995, **23**, 239-247.
32. Z. Shuxian, W. K. Hall, G. Ertl and H. Knözinger, *J. Catal.*, 1986, **100**, 167-175.
33. Y. An, B. Huang, Z. Wang, X. Long, Y. Qiu, J. Hu, D. Zhou, H. Lin and S. Yang, *Dalton Trans*, 2017, **46**, 10700-10706.
34. J. Deng, P. Ren, D. Deng and X. Bao, *Angew. Chem. Int. Ed. Engl.*, 2015, **54**, 2100-2104.
35. K. Fukui, *Science*, 1982, **218**, 747-754.
36. F. D. Mango, in *Advances in Catalysis*, Elsevier, 1969, vol. 20, pp. 291-325.
37. M. Gong, W. Zhou, M.-C. Tsai, J. Zhou, M. Guan, M.-C. Lin, B. Zhang, Y. Hu, D.-Y. Wang and J. Yang, *Nat. Commun*, 2014, **5**, 4695.
38. D. Harrington and B. Conway, *Electrochim. Acta*, 1987, **32**, 1703-1712.
39. C. Tsai, H. Li, S. Park, J. Park, H. S. Han, J. K. Norskov, X. Zheng and F. Abild-Pedersen, *Nat Commun*, 2017, **8**, 15113.
40. A. Damian and S. Omanovic, *J. Power Sources*, 2006, **158**, 464-476.
41. Z. Rotenberg, *J. Electroanal. Chem.*, 1993, **345**, 469-474.